ChemPubSoc Europe

DOI: 10.1002/chem.201504903

CHEMISTRY A European Journal Full Paper

Boron Difluoride Complexes

Boron Difluoride Curcuminoid Fluorophores with Enhanced Two-Photon Excited Fluorescence Emission and Versatile Living-Cell Imaging Properties

Kenji Kamada,*[a, b] Tomotaka Namikawa,[b] Sébastien Senatore,[c] Cédric Matthews,[c] Pierre-François Lenne,[c] Olivier Maury,[d] Chantal Andraud,[d] Miguel Ponce-Vargas,[e] Boris Le Guennic,[e] Denis Jacquemin,[f, g] Peter Agbo,[h] Dahlia D. An,[h] Stacey S. Gauny,[h] Xin Liu,[h] Rebecca J. Abergel,*[h] Frédéric Fages,[i] and Anthony D'Aléo*[i]

Abstract: The synthesis of boron difluoride complexes of a series of curcuminoid derivatives containing various donor end groups is described. Time-dependent (TD)-DFT calculations confirm the charge-transfer character of the second lowest-energy transition band and ascribe the lowest energy band to a "cyanine-like" transition. Photophysical studies reveal that tuning the donor strength of the end groups allows covering a broad spectral range, from the visible to the NIR region, of the UV–visible absorption and fluorescence spectra. Two-photon-excited fluorescence and Z-scan techniques prove that an increase in the donor strength or in the rigidity of the backbone results in a considerable increase in the two-photon cross section, reaching 5000 GM, with predominant two-photon absorption from the S_0–S_2 charge-transfer transition. Direct comparisons with the hemicurcuminoid derivatives show that the two-photon active band for the curcuminoid derivatives has the same intramolecular charge-transfer character and therefore arises from a dipolar structure. Overall, this structure–relationship study allows the optimization of the two-photon brightness (i.e., 400–900 GM) with one dye that emits in the NIR region of the spectrum. In addition, these dyes demonstrate high intracellular uptake efficiency in Cos7 cells with emission in the visible region, which is further improved by using porous silica nanoparticles as dye vehicles for the imaging of two mammalian carcinoma cells type based on NIR fluorescence emission.

Introduction

Two-photon absorption has become a widely used technique enabling in-depth optical bioimaging,[1] photodynamic therapy,[2] drug delivery,[3] three-dimensional microfabrication,[4] optical limiting,[5] and three-dimensional data storage.[6] In the particular field of two-photon-excited fluorescence (TPEF) spectroscopy and microscopy, there is an increasing demand for new small molecule two-photon probes for cell-imaging purposes.[7]

From the optical point of view, the main figure of merit for such fluorophores is the two-photon (TP) brightness (B^2). It is defined as the product of the two-photon absorption (TPA) cross section (σ^2) and the fluorescence quantum yield (Φ_f), and

[a] Dr. K. Kamada
IFMRI
National Institute of Advanced Industrial Science and Technology
Ikeda, Osaka 563-8577 (Japan)
E-mail: k.kamada@aist.go.jp

[b] Dr. K. Kamada, T. Namikawa
Department of Chemistry, School of Science and Technology
Kwansei Gakuin University, Sanda, Hyogo 669-1337 (Japan)

[c] Dr. S. Senatore, Dr. C. Matthews, Dr. P.-F. Lenne
Aix Marseille Université, CNRS
Institutde Biologie du Développement de Marseille
UMR7288, 13288 Marseille 9 (France)

[d] Dr. O. Maury, Dr. C. Andraud
Université Lyon 1, ENS Lyon, CNRS, UMR 5182, 69364 Lyon (France)

[e] Dr. M. Ponce-Vargas, Dr. B. Le Guennic
Institut des Sciences Chimiques de Rennes
UMR 6226 CNRS, Université de Rennes 1
263 Avenue du Général Leclerc, 35042 Rennes Cedex (France)

[f] Prof. D. Jacquemin
Laboratoire CEISAM, UMR CNRS 6230, Université de Nantes
2 Rue de la Houssinière, BP 92208, 44322 Nantes Cedex 3 (France)

[g] Prof. D. Jacquemin
Institut Universitaire de France, 1 Rue Descartes
75005 Paris Cedex 05 (France)

[h] Dr. P. Agbo, Dr. D. D. An, Dr. S. S. Gauny, Dr. X. Liu, Dr. R. J. Abergel
Chemical Sciences Division, Lawrence Berkeley National Laboratory
Berkeley, CA 94720 (USA)
E-mail: rjabergel@lbl.gov

[i] Prof. F. Fages, Dr. A. D'Aléo
Aix Marseille Université, CNRS, CINaM UMR 7325
Campus de Luminy, Case 913, 13288 Marseille (France)
E-mail: daleo@cinam.univ-mrs.fr

Supporting information for this article is available on the WWW under http://dx.doi.org/10.1002/chem.201504903; containing all NMR spectra, additional photophyiscal spectra and data.

its optimization therefore requires the simultaneous consideration of both parameters.[8] TPEF has the advantage of using incident near-infrared (NIR) photons, enabling, amongst others, the selective excitation of the molecular probe in the biological transparency window. Concomitantly, it is highly desirable to collect emitted photons in the same wavelength range and this leads to the emergence of the so-called NIR-to-NIR probes. However, the compounds reported to date showed small TP brightness values.

TPEF has been reported for boron difluoride-containing dyes, such as boron-dipyrromethene (BODIPY)[5c,9] or those based on other types of N^N ligands.[10] However, much less is known about the behavior of O^O analogues. Jullien and coworkers have shown that BF_2 complexes of dibenzoylmethane derivatives are TP active with significant values of the TPA cross section.[11] Recently, we[12] and others[13] described the synthesis and solution photophysics of boron difluoride complexes of curcuminoids as efficient dyes absorbing and emitting visible light in solution. Their molecular structures feature two terminal electron-donor (D) groups, and a central dioxaborine ring playing the role of a strong electron-acceptor (A) unit. As such, they display a D–A–D sequence found in centrosymmetric and non-centrosymmetric TP chromophores. Further, we reported the NIR-to-NIR optical signature of nanoparticles of two boron difluoride complexes of curcuminoid derivatives.[14]

Following those previous investigations, we decided to explore the possibility of tagging cells by using boron difluoride complexes of curcuminoid derivatives and image them by using NIR-to-NIR techniques. We describe herein a series of boron difluoride complexes of curcuminoids (i.e., **1**-BF_2–**8**-BF_2, Scheme 1) including the compounds **1**-BF_2–**4**-BF_2, in which we introduced amino-substituted aryl termini as strong donor groups. Compound **3**-BF_2 contains an *n*-propyloxy chain at the *ortho* position of the double bond, which reinforces the donor strength with respect to compound **1**-BF_2. The dye **2**-BF_2 incorporates a cyclohexanone unit, which imposes conformational restrictions to the curcuminoid backbone as compared to compound **1**-BF_2. The dye **4**-BF_2 possesses a julolidine group whose donor strength is reportedly high because of the planarity of the amino group substituent.[15] As a matter of fact, increasing the excited-state charge-transfer (CT) character was expected to shift the emission color to the far red or NIR region, and to enhance the TPA cross section. For the spectroscopic studies, we used compound **5**-BF_2–**8**-BF_2 as reference dyes displaying a weaker donor group. Noticeably, compound **7**-BF_2 contains two short oligoethylene glycol (OEG) chains that make this compound hydrosoluble and compound **8**-BF_2 is based on the naturally occurring curcumin. We carried out a detailed experimental study, by using TPEF and Z-scan techniques, combined with a time-dependent (TD)-DFT theoretical approach, of TPA absorption of the dyes, which allowed us to decipher the features that characterize their linear and non-linear optical properties. To this end, the hemicurcuminoid complexes M**1**-BF_2 and M**6**-BF_2 that behave as dipolar dyes were useful in order to assign the origin of the mismatch between the lowest energy absorption bands recorded in the one- and two-photon excitation modes.[9d,10]

We show that very large TPA cross-section scan be obtained, up to 5000 GM for **4**-BF_2,a compound that also features NIR fluorescence emission with high TP brightness in solution. Using **3**-BF_2, **4**-BF_2, and**7**-BF_2, which exhibit key attributes in terms of TP brightness and NIR-to-NIR behavior for the two former, we propose versatile strategies for living-cell imaging.

Results and Discussion

Design and synthesis

The synthesis of all curcuminoid derivatives *n*-H ($n=1$–8), except for compound **2**-H, was performed as reported elsewhere.[12] The hemicurcuminoid models were synthesized in a similar manner but by using only one equivalent of the appropriate aldehyde to avoid the second substitution.[16] Derivative **2**-H was prepared following a previously published procedure.[17] Briefly, 2-acetylcyclohexanone, 4-(*N*-dimethyl)aminobenzaldehyde, boric acid, and a catalytic amount of morpholine and acetic acid were mixed in the absence of solvent. The sample was irradiated for two minutes at 200 °C under atmospheric pressure in a microwave reactor. After cooling to room temperature, the resulting solid was sonicated for 1 h in ethyl acetate and filtered through a glass filter. The solid was washed with ethanol and pentane, yielding the pure ligands. The boron difluoride complexes were prepared according to our previous reports[12] except for the amino derivatives (i.e., compounds **2**-BF_2, **3**-BF_2, and **4**-BF_2) that required the use of only 1.1 equivalent of boron trifluoride etherate. The latter complexes were purified by flash chromatography.

X-Ray crystallography was performed on the ligands **3**-H and **4**-H, for which crystals were obtained by slow evaporation of a mixture of ethyl acetate and cyclohexane (1:3).[18] Detailed crystallographic parameters are included in Table S1 in the Supporting Information. Whereas the ligand **3**-H ($I\bar{4}$, $Z=8$) crystallizes in the tetragonal system, the ligand **4**-H ($Pna2_1$, $Z=4$) crystallizes in an orthorhombic space group. The ligands **3**-H and **4**-H are observed to prevail as the keto–enol form in the crystal and are non-planar structures. The π-conjugated backbone of compound **3**-H shows a strong curvature, which results in a significant difference in the bond lengths between the C1–C11 (1.369 Å) and C1–C2 (1.401 Å) bonds (Figure 1 a), suggesting a localized double bond in the keto–enol moiety of the π-conjugated backbone. In the case of compound **4**-H, the heptadiene keto–enol fragment is fully planar, which leads to similar bond lengths for the C1–C17 (1.391 Å) and C1–C2 (1.402 Å) bonds (Figure 1 b), indicating an effective π delocalization within this fragment. However, the planes of the terminal phenyl rings are twisted with respect to each other around the heptadiene keto–enol part with an angle of approximately 30°. In solution, an efficient delocalization in all ligands and complexes can be unambiguously evidenced by looking at the ^{13}C NMR spectra (see the NMR spectra in the Supporting Information) where isochronous signals for the C=O and C–O–R (R = H or BF_2) moieties are obtained.

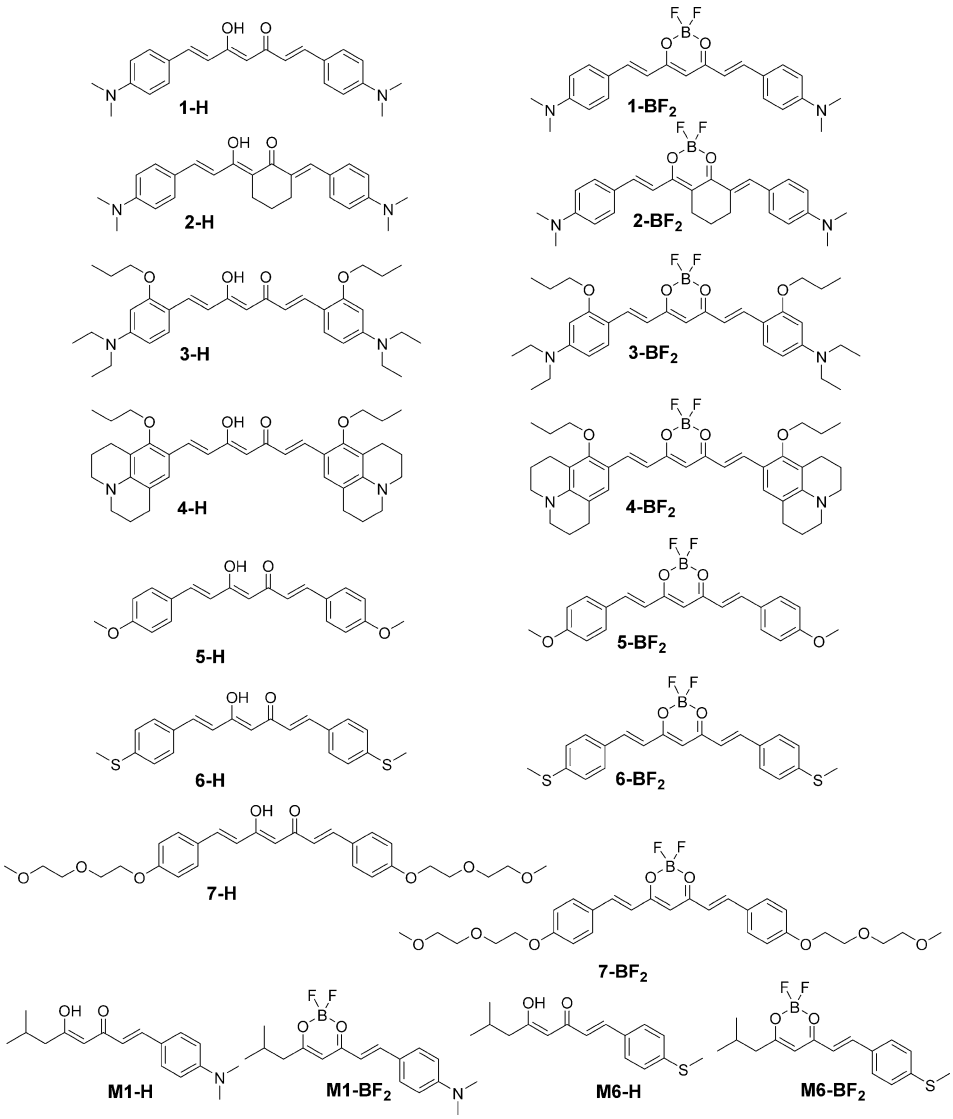

Scheme 1. Structures of the curcuminoid ligands *n*-H ($n=1$–8), M**1**-H, and M**6**-H, and the corresponding boron difluoride complexes *n*-BF_2 ($n=1$–8), M**1**-BF_2, and M**6**-BF_2.

All boron difluoride dyes were found to be chemically and photochemically stable in solution and in the solid state. More specifically, BF_2 decoordination was not observed in any of the investigated solvents, even in the presence of protic ones.[14,19] Notably, compound **7**-BF_2 was found to be slightly soluble in water at concentrations lower than 4×10^{-7} M and no BF_2 release was observed within 48 h.

One-photon optical properties

The electronic UV–visible absorption and fluorescence emission spectra were recorded in dichloromethane solution (Figures S1–S3 in the Supporting Information for the ligands and Figure 2 and Figures S4 and S5 in the Supporting Information for the boron difluoride complexes) and the spectroscopic data are summarized in Table S2 in the Supporting Information for the ligands and in Table 1 for the boron difluoride complexes. The UV–visible absorption maxima of the curcuminoid ligands span wavelengths from $\lambda=414$ to 520 nm (for compounds **7**-H and **4**-H, respectively) in dichloromethane, shifting toward the red part of the spectrum upon increasing the donor strength, as expected. The associated molar absorption coefficients are large ($\varepsilon>54\,000\ M^{-1}cm^{-1}$). For the hemicurcuminoids M*n*-H, the same trend is observed with ε values about half of those of their respective parent curcuminoid derivatives *n*-H. Upon complexation to boron difluoride, all curcuminoid derivatives experience a red shift of their absorption maxima from $\tilde{\nu}=3530\ cm^{-1}$ (for compound **3**-BF_2) to $\tilde{\nu}=4065\ cm^{-1}$ (for compound **2**-BF_2). The same effect is observed for both hemicurcuminoid derivatives. Such shift results in chromophores presenting similar band shapes in the range $\lambda=500$–650 nm. The low energy band is rather narrow and can be attributed to a π–π^* transition as discussed elsewhere.[12] As for the free ligands, the absorption band of the dipolar BF_2-containing hemicurcuminoid derivatives is more red shifted for the structures incorporating the strongest donor groups.

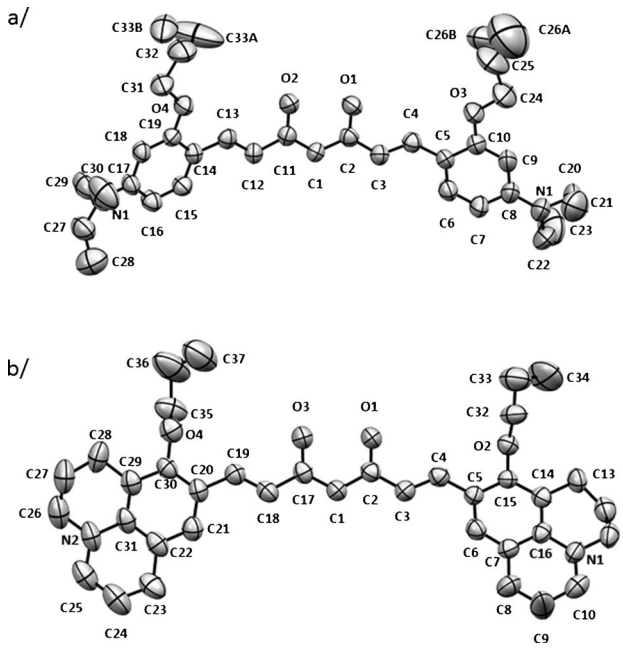

Figure 1. Molecular structures (ORTEP) of compounds: a) **3**-H, and b) **4**-H with displacement ellipsoids drawn at the 50% probability level. Hydrogen atoms have been omitted for clarity.

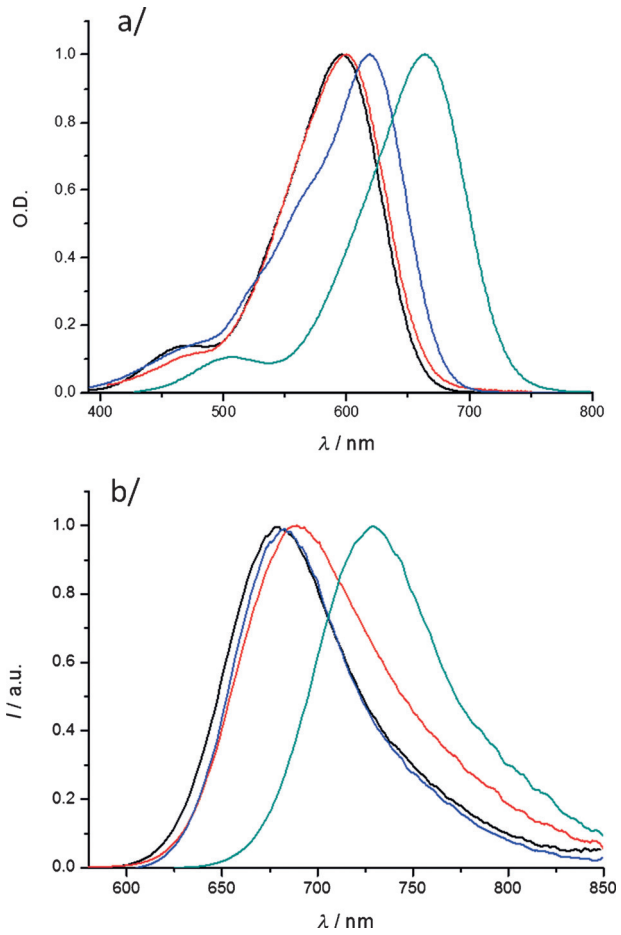

Figure 2. a) Electronic absorption spectra (10^{-5} M), and b) corrected fluorescence emission spectra (10^{-6} M, λ_{exc} at the absorption maximum) of **1**-BF_2 (black lines), **2**-BF_2 (red lines), **3**-BF_2 (blue lines), and **4**-BF_2 (turquoise lines) in dichloromethane at room temperature. All spectra are normalized.

Unlike the 2′-hydroxychalcone derivatives that show fluorescence emission quenching due to a fast excited state intramolecular proton transfer (ESIPT) phenomenon,[19a,20] the curcuminoid ligands are remarkably emissive in solution (Figures S1 and S2 and Table S2 in the Supporting Information) with emission at lower energies compared to those of the 3-hydroxyflavone compounds.[21] The ligands studied here exhibit emissions in the visible (from $\lambda = 473$ to 621 nm) and fluorescence quantum yields up to 30%. The emissions are associated with large Stokes shifts ranging from about $\tilde{\nu} = 3000$–$3500\ cm^{-1}$ in the case of the curcuminoid ligands to even larger values for the hemicurcuminoid derivatives (i.e., $\tilde{\nu} = 4600\ cm^{-1}$).

As observed with the ligands, both the UV–visible absorption and emission of the BF_2 complexes shift bathochromically when increasing the donor strength of the lateral substituents. They were found fluorescent in the region $\lambda = 540$–730 nm with fluorescence quantum yields ranging from 13 to 55% in dichloromethane. Taking compound **6**-BF_2 (i.e., a thioether) as

Table 1. Spectroscopic data and photophysical properties of compounds *n*-BF_2 ($n = 1$–8) and M*n*-BF_2 ($n = 1$ and 6) in dichloromethane at room temperature.[a]

Compound	UV/Vis		Fluorescence						
	λ_{abs}	ε_{max}	λ_{em}	$\Delta\tilde{\nu}_{ST}$	Φ_f [%]	$\Phi_f \times \varepsilon$	τ_f	k_f	k_{nr}
1-BF_2	597	48400	683	2109	42.5	20570	1.94	2.2	3.0
2-BF_2	601	98800	690	2146	14	13832	0.86	1.6	9.9
3-BF_2	619	59900	683	1514	39	23361	2.13	1.8	2.9
4-BF_2	648	101200	728	1696	13.5	13662	1.02	1.3	8.5
5-BF_2	488	78500	538	1904	44	34540	1.30	3.4	4.3
6-BF_2	503	86200	587	2845	55	47410	1.95	2.8	2.3
7-BF_2	488	73200	538	1904	44	32208	1.55	3.4	4.3
8-BF_2	500	76750	560	2143	34.5	26479	0.99	3.5	6.6
M**1**-BF_2	500	39500	572	2517	3.5	1383	<0.7	–	–
M**6**-BF_2	423	23700	521	4447	5.5	1304	<0.7	–	–

[a] Absorption maximum wavelength λ_{abs} [nm], molar absorption coefficients ε_{max} [$M^{-1}cm^{-1}$], fluorescence maximum wavelength λ_{em} [nm], Stokes shifts $\Delta\tilde{\nu}_{ST}$ [cm^{-1}], fluorescence quantum yields Φ_f, brightness $\Phi_f \times \varepsilon$ [$M^{-1}cm^{-1}$], fluorescence lifetimes τ_f [ns], radiative k_f rate constants [$10^8\ s^{-1}$], and non-radiative $k_{nr} = (1-\Phi_f)/\tau_f$ [$10^8\ s^{-1}$] rate constants.

a reference, a bathochromic shift of 94 nm (i.e., 3130 cm^{-1}) is observed compared to compound **1**-BF_2that bears a dialkylamino group. The same trend is found when replacing the diethylamino donor group with the geometrically constrained julolidine group, resulting in fluorescence emission in the NIR region ($\lambda = 730$ nm) for compound **4**-BF_2. The small red shifts of both the absorption and emission spectra of compound **2**-BF_2 relative to compound **1**-BF_2 may be a consequence of the presence of the cyclohexyl group that would impose a more planar structure to the curcumnoid backbone. However, a significant quenching of the singlet excited state is observed, which is contrary to what would be expected in the case of a rigidification of the molecular structure. Although this effect remains unclear, it shows that the presence of a cyclohexyl unit leads to an opening of non-radiative deactivation channels. The emission spectra of the hemicurcuminoids M**1**-$BF_2$and M**6**-BF_2 are far less shifted than those of the parent compounds **1**-$BF_2$and **6**-BF_2, respectively. The fluorescence quantum yields in dichloromethane are lower (i.e., 3.5 and 5.5% for M**1**-BF_2 and M**6**-BF_2, respectively) as compared to the curcuminoids. Both curcuminoid and hemicurcuminoid boron difluoride complexes exhibit rather small Stokes shifts when compared to those of the corresponding free ligands ($\approx$2000 cm^{-1}) suggesting a more limited structural relaxation in the excited state.

The solvent dependences of the absorption and emission properties were examined for compounds *n*-BF_2 ($n = 1$–4, 6, and 7) as well as for both hemicurcuminoids M**1**-BF_2 and M**6**-BF_2, to gain insights into the influence of the donor groups (Figure 3, Figures S6–S13 and Tables S3–S6 in the Supporting Information). Both UV–visible absorption and fluorescence emission spectra of these compounds show positive solvatochromism, the vibronic structure disappearing in the more polar solvents. The solvent-induced bathochromic shift of the absorption band ranges from 530 (for compound **6**-BF_2) to 1970 cm^{-1}(for compound **3**-BF_2). This positive solvatochromic shift of the absorption bands indicates that the local excited state S_1 is more polar than its ground state S_0 counterpart. Furthermore, the variation of the solvent-induced bathochromic shift suggests that the difference of the dipole moments is strongly linked to the strength of the donor group. Correlations between the Stokes shifts and the polarity function ($\Delta f'$)of the solvent yield linear plots with positive slopes (Figures S14 and S15 in the Supporting Information).[22] This trend confirms the relaxation toward a solvent-equilibrated singlet excited state with a charge-transfer character and shows that the excited-state dipole moment is larger than the ground-state one. This behavior is in agreement with what was observed for other curcuminoid boron difluoride compounds[12,13c] and is related to the strong electron-withdrawing effect of the central difluoro dioxaborine chelate.[23] These data evidence the strong charge transfer character of the curcuminoid dyes.[24]

The rate constants of the radiative and the non-radiative deactivation pathways are listed in Tables S3–S6 in the Supporting Information. As observed with other curcuminoid boron difluoride derivatives,[12] the radiative constants k_f were found independent of the solvent nature. There is therefore no increase of the fluorescence transition moment with an increasing polarity of the solvent, which is consistent with a limited nuclear reorganization in the relaxed emitting state with respect to the Franck–Condon excited state.[22] In marked contrast, the non-radiative constant values (k_{nr}) decrease with increasing solvent polarity, indicating that non-radiative processes are less efficient in polar solvents. For highly polar solvents, such as acetone and acetonitrile, the increase in the k_{nr} value may be due to the energy gap law.[25] Even if it is built on a more rigid structure due to its cyclohexyl group, compound **2**-BF_2 displays slightly lower k_f values but k_{nr} values more than twice larger than those of compound **1**-BF_2, which can be attributed to the conformational preference imposed by the cyclohexyl cycle that alters the ground- and excited-state properties.

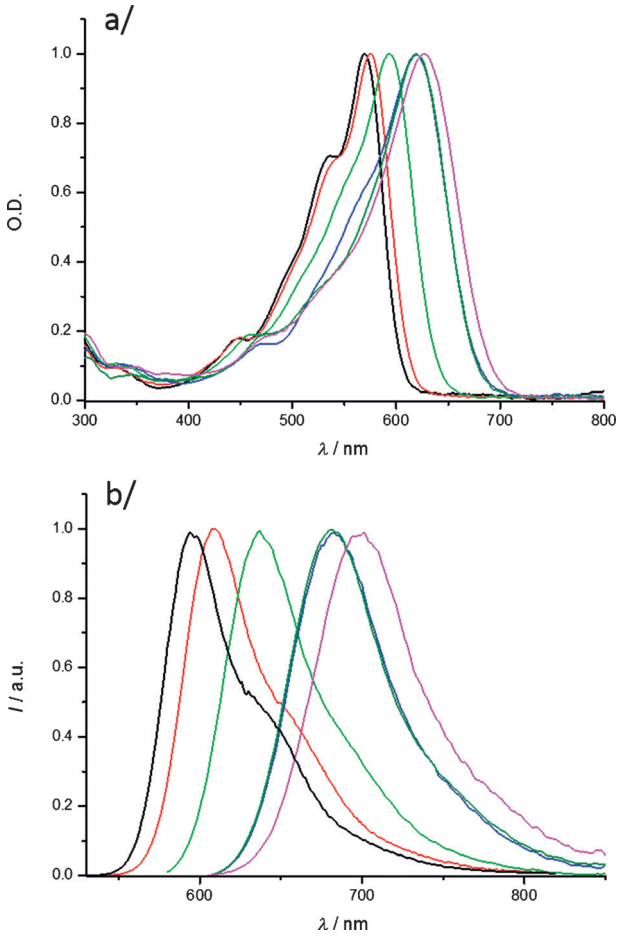

Figure 3. a) Normalized electronic absorption, and b) fluorescence emission spectra of compound **4**-BF_2 in solvents of different polarity at room temperature ($\lambda_{exc} = 560$–610 nm, *n*-dibutyl ether (black lines), ethylic ether (red lines), ethyl acetate (green lines), dichloromethane (blue lines), butyronitrile (turquoise lines), and acetonitrile (magenta lines).

The OEG chain-bearing complex **7**-BF_2displays the same properties in organic solvents than its parent methylated compound **5**-BF_2.[12] Furthermore, the photophysical properties of compound **7**-BF_2 could be measured in aqueous solution and revealed absorption and emission maximum wavelengths at $\lambda = 471$ and 631 nm, respectively, which is consistent with the

high polarity of water (Figure S11 in the Supporting Information).[12] The fluorescence quantum yield reaches a value of 8%, with a fluorescence lifetime shorter than 0.7 ns, resulting in a brightness of 5760 $M^{-1}cm^{-1}$.

Two-photon optical properties

The TPA absorption cross sections of the studied compounds were determined by using both TPEF and Z-scan techniques. The combined use of both techniques provided a more precise determination of the TPA cross section.[26] TP-induced emission and excitation spectra were recorded in the wavelength range $\lambda = 700–1000$ nm by using a femtosecond Ti–sapphire pulsed laser source, according to the experimental protocol described by Webb and Xu,[9a] whereas open-aperture Z-scan traces were recorded from $\lambda = 650$ to 1050 nm by using a femtosecond optical parametric amplifier pumped by a Ti–sapphire regenerative amplifier, according to the experimental protocol described by Sheik-Bahae et al.[27] with the reported setup.[27b] The observation of a quadratic dependence of the fluorescence intensity versus the incident laser power at several wavelengths in the TPEF experiments (Figure S16 in the Supporting Information) unambiguously confirmed that the origin of the fluorescence emission can be assigned to a TP absorption process (Figure S16 in the Supporting Information). In the experimental laser power range used for these TPEF measurements, we checked that no saturation or photobleaching occurred. The TP cross sections of all curcuminoid derivatives were measured by TPEF and calibrated by using rhodamine B,[28] zinc-2,9,16,23-tetra-*tert*-butyl-29*H*,31*H*-phthalocyanine,[29] and styryl 9M[30] as references depending on the TP absorption maximum, whereas an "in-house" standard compound (i.e., MPPBT, 1,4-Bis(2,5-dimethoxy-4-{2-[4-(*N*-methyl)pyridin-1-iumyl]ethenyl}-phenyl)butadiyne triflate) was used for the Z-scan measurements.[31] The TP excitation spectra are presented in Figures S22–S30 in the Supporting Information for the ligands and in Figure 4 and Figures S17–S21 in the Supporting Information for the complexes. The TP absorption maxima, cross sections and brightness of the ligands and complexes are reported in Table S7 in the Supporting Information and in Table 2, respectively. As a representative example, the ligand **8**-H shows a TPA absorption maximum at $\lambda = 720$ nm in dichloromethane by using the TPEF approach or at $\lambda = 707$ nm in chloroform by using the Z-scan technique with a σ^{TPA} value of 115 or 157 GM, respectively. Those values are comparable for both techniques and are in agreement with the values reported elsewhere by Hernández et al. (≈ 90 GM at $\lambda = 740$ nm).[32]

As can be readily seen from the spectra obtained for the ligands (i.e., *n*-H) and the corresponding boron difluoride derivatives (i.e., *n*-BF_2), the TPA band is strongly blue shifted compared to the one-photon absorption (OPA) band and clearly does not match the S_0–S_1 transition. According to the TPA selection rules, this behavior is characteristic of centrosymmetric D–A–D chromophores[5d,24,33] but it is also observed for other specific non-centrosymmetric compounds including boron difluoride dyes such as BODIPY,[5c,9c] as well as in polymethine dyes.[10] This effect is generally assigned to a TP-active transition lying at higher energy,[33b] and/or to the localization of the excitation in one of the two halves of the chromophore as a result of vibration- or polar solvation-induced symmetry breaking in the ground or excited states, as rationalized for polymethine derivatives.[5d,24,33a] Here, we show that the observed TPA absorption corresponds to the S_0–S_2 transition and this was verified through TD-DFT calculation for compound **1**-BF_2 (see the next section). A similar effect was reported by others in the case of the curcumin **8**-H,[32] for which a blue shift of the TPA relative to the OPA was observed. Indeed, the more TP-active transition is the S_0–S_2 transition due to its stronger CT character compared to the cyanine-like S_0–S_1 transition. However, and similarly to the polymethine derivatives[5d,24,33a] and to the curcumin **8**-H,[32] the lowest-energy transition is not completely TPA forbidden and a weak σ^{TPA} value of approximately 10–40 GM in that wavelength range was measured for the dyes **5**-BF_2,[14] **6**-BF_2, and **7**-BF_2 in dichloromethane. Those low-energy TPA transitions could not be observed in compound **1**-BF_2, **2**-BF_2, **3**-BF_2, and **4**-BF_2 because the OPA is too shifted in the red region to be monitored with our TPEF setup.[34]

To gain insights into the TPA process, we also measured the TPA properties of the hemicurcuminoid models that were suitable for TPEF experiments according to the possibilities of our experimental setup. Note that the hemicurcuminoids analogous of compound **5** containing anisole as donor group were also prepared but their low fluorescence quantum yields in dichloromethane precluded such measurement. The compounds (M*n*-H and M*n*-BF_2 with $n = 1$ and 6) showed an approximately fivefold decrease of the TPA cross section compared to their respective curcuminoid counterparts. However, their TPA band perfectly matched the S_0–S_1 OPA transitions (Figures S20 and S21 as well as S29 and S30 in the Supporting Information). This is the result of the typical dipolar structure and is demonstrated by theoretical calculations (see below). Interestingly, the spectra of compound **1**-BF_2 and M**1**-BF_2 (**1**-H and M**1**-H) as well as **6**-BF_2 and M**6**-BF_2 (**6**-H and M**6**-H) present similar TPA spectra with the maxima almost lying at the same energy. This observation indicates that the TPA spectral signatures of both curcuminoid ligands and their boron difluoride-containing species have a dipolar character, which is reflected by the fact that the HOMO−1 of compound **1**-BF_2 is one part of the linear combination of the lower moieties of the HOMO of M**1**-BF_2. In the same way, the LUMO of compound **1**-BF_2 is the lower part of the linear combination of two moieties of the LUMO of M**1**-BF_2 (Figure 5).

The TPA properties are very sensitive to the nature of the donor end group and the planarity of the conjugated skeleton. Whereas the alkoxy-substituted dye **7**-H shows a TPA maximum around $\lambda = 720$ nm with a σ^{TPA} value of approximately 90 GM, the amino analogue **1**-H is shifted to $\lambda = 840$ nm with a σ^{TPA} of ca. 225 GM, whereas **6**-H containing an intermediate thio-ether donor shows a σ^{TPA} value of approximately 205 GM and a maximum at approximately $\lambda = 730$ nm.

The strength of the TPA reaches its maximum for the ligand **4**-H, which features the strongest donor group ($\lambda = 860$ nm with a σ^{TPA} value of ≈ 515 GM). Similarly to the ligands, the thi-

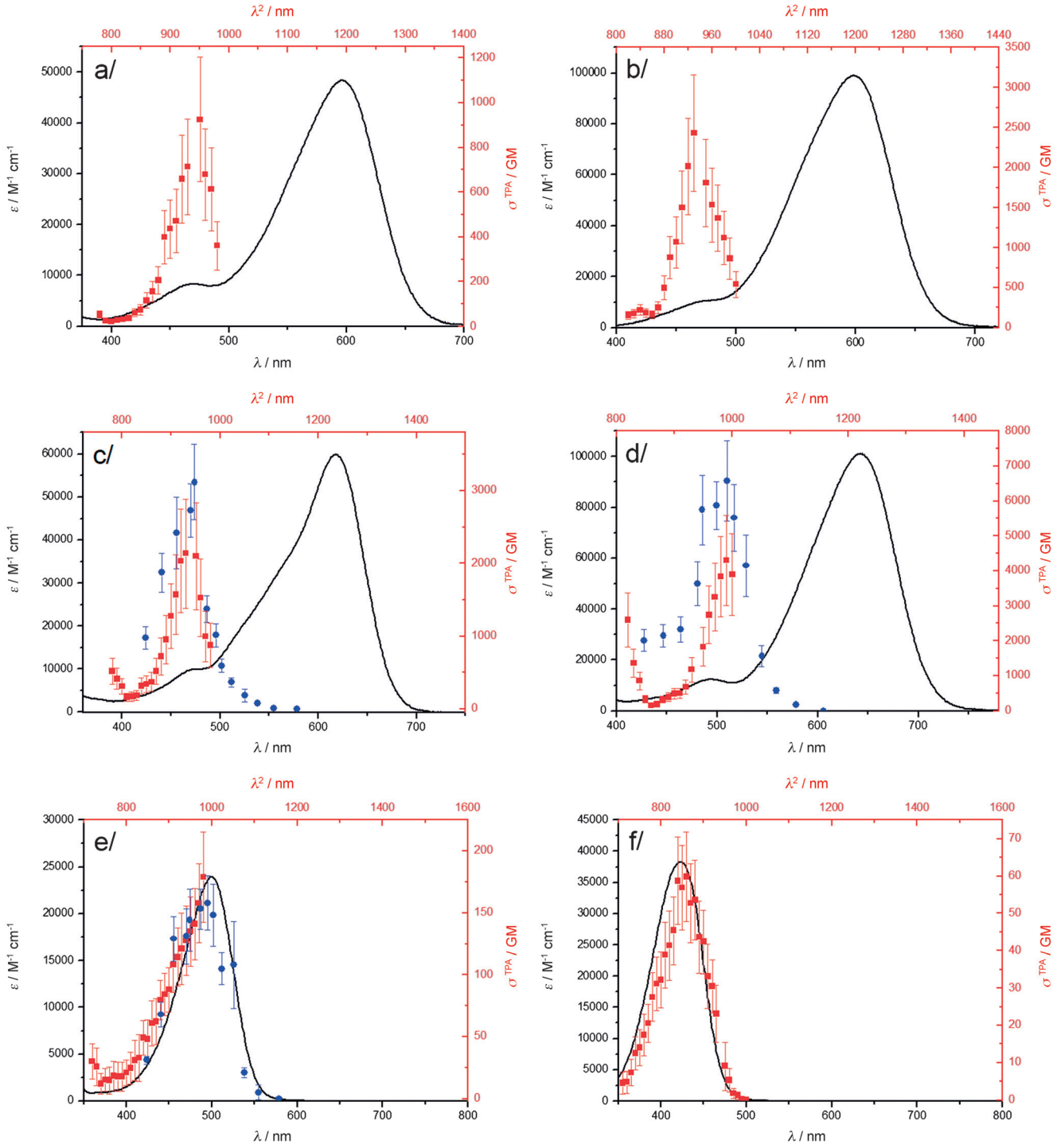

Figure 4. Two-photon excitation (red squares = top *x* axis and red lines = right *y* axis) and Z-scan (blue circles = top *x* axis and red lines = right *y* axis) with their error bars, OPA spectra (black lines = bottom *x* axis and black lines = left *y* axis) in dichloromethane. a) **1**-BF_2, b) **2**-BF_2, c) **3**-BF_2, d) **4**-BF_2, e) M**1**-BF_2, and f) M**6**-BF_2.

oanisole-containing boron difluoride complex (i.e., compound **6**-BF_2) shows a TP excitation maximum around $\lambda = 820$ nm with a TPA cross section of approximately 330 GM, whereas the dimethylamino analogue (i.e., compound **1**-BF_2) absorbs at $\lambda = 950$ nm with a TPA cross section of approximately 610 GM. Noticeably, the TPA spectra of the boron difluoride dyes are red shifted in comparison to the curcuminoid ligands, which is in agreement with the experimental data found for the OPA. Compounds **5**-BF_2[12] and **7**-BF_2, bearing anisole donor groups, display similar emission maxima at $\lambda = 770$ nm and TPA cross sections of 160 GM. Although the TPEF of compound **7**-BF_2 in water was detected when increasing the power of the laser, no TPA could be detected because of the low concentration level needed to avoid aggregation in water.

Table 2. Two-photon absorption maxima, cross sections, and brightness of the boron difluoride complexes of curcuminoid and hemicurcuminoid in dichloromethane.

	1-BF_2	**2**-BF_2	**3**-BF_2	**4**-BF_2	**5**-BF_2	**6**-BF_2	**7**-BF_2	**8**-BF_2	M**1**-BF_2	M**6**-BF_2
λ^2_{abs} [nm]	950	950	940 (950)[a]	990 (990)[a]	770	820	770	810	980 (990)[a]	860
σ^{TPA} [GM]	925	2430	2135 (3110)[a]	4270 (6580)[a]	155	330	160	225	179 (159)[a]	60
B^2_{max} [GM]	389	340	833 (1213)[a]	576 (888)[a]	68	182	70	78	7 (6)[a]	3

[a] Measured by using the Z-scan technique.

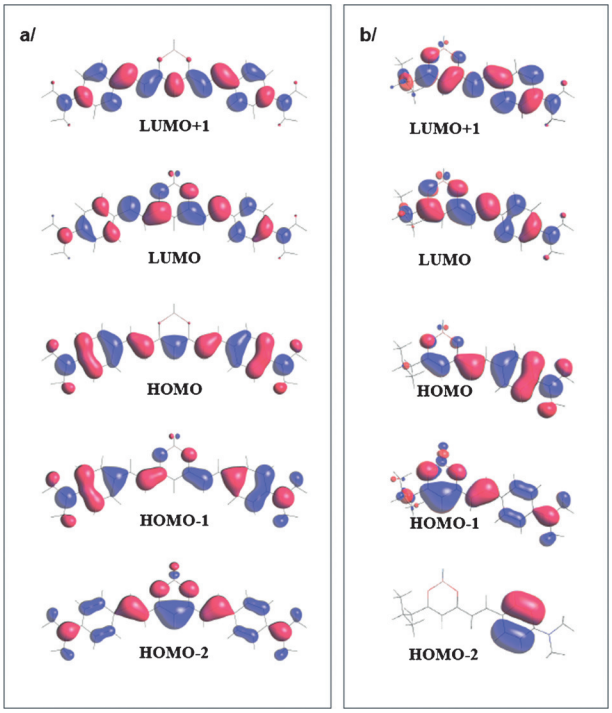

Figure 5. HOMO−2, HOMO−1, HOMO, LUMO, and LUMO+1 of: a) **1**-BF_2, and b) M**1**-BF_2.

The effect of the donor strength on both the emission wavelength and the TPA cross section is further evidenced when comparing the complex **3**-BF_2 with the stronger donor-containing compound **4**-BF_2. The latter displays a twofold increase of the TPA cross section, reaching 5000 GM, but has a similar brightness because its fluorescence quantum yield simultaneously drops by the same factor. Further information on the structure–TPA properties relationships is gathered by comparing the complexes **1**-BF_2 and **2**-BF_2. The TPA cross section is increased by almost a factor three in favor of compound **2**-BF_2, most probably due to the higher planarity of the latter structure.

TD-DFT calculations

To identify the nature of the S_0–S_1 and S_0–S_2 transitions and to confirm that the S_0–S_2 transition is the active transition in the TPA processes, theoretical calculations were performed on **1**-BF_2 and M**1**-BF_2, which were taken as representative compounds for D–A–D and dipolar hemicurcuminoid structures, respectively. DFT and TD-DFT calculations were performed by using the standard B3LYP/6-31G(d) level of theory[35] (see the Experimental Section).

For compound **1**-BF_2, the S_0–S_1 and S_0–S_2 bands are rather close on the energy scale (2.247 and 2.752 eV, i.e., 552 and 451 nm, respectively, in dichloromethane, Table 3). The S_0–S_1 transition mainly corresponds to the HOMO→LUMO transition (Figure 5a), where the electronic density of the HOMO is spread over the whole backbone. This type of HOMO orbital can be ascribed as a "cyanine-like" transition[36] due to the odd number of sp^2-hybridized C atoms in the conjugated skeleton with the electronic density equally distributed from one donor to the other. The S_0–S_2 transition is a mixture of HOMO−1→LUMO and HOMO→LUMO+1 transitions, with the major contribution involving the former. For the HOMO−1→LUMO mono-electronic transition, the HOMO−1 has its electronic density on the dimethylaniline moiety, whereas the LUMO is mostly localized on the dioxaborine ring. This feature indicates a charge-transfer character of the S_0–S_2 transition resulting in dyes having a bis-dipole type of electronic structure,[37] which leads to a high TPA cross section as evidenced by TPEF experiments. It is worth noting that both the HOMO−1 and the LUMO display a nodal plane containing the BF_2 unit and the *meso*-carbon atom.[23] In the vertical approximation, the calculated oscillator strength of the S_0–S_1 band is 2.277, whereas that of S_0–S_2 transition is 32 times lower (i.e., 0.072), which is in agreement with the OPA experimental spectra (see above).

For compound M**1**-BF_2, the TD-DFT calculated S_0–S_1 and S_0–S_2 transitions are more separated than for compound **1**-BF_2 (2.731and 3.981 eV, i.e., 454 and 312 nm, respectively, Table 3), which parallels the experimental spectrum. The S_0–S_1 band is mainly represented by the HOMO→LUMO transition (Figure 5b), where the HOMO shows the electronic density on the aniline moiety and the LUMO is mainly centered on the acacBF_2 (acac = acetylacetonate) part, therefore presenting a strong CT character. For such dipolar boron difluoride complexes, the S_0–S_2 transition has a strong HOMO−1→LUMO contribution.

To simulate the UV–visible absorption spectra and the TPA spectra[38] of **1**-BF_2 and M**1**-BF_2, we calculated the transition dipole moments between the ground and excited states by using the Tamm–Dancoff approximation[39] (TDA) for the TD-DFT calculation at the B3LYP/6-31G(d) level of theory (Figure 6). The results of the TDA B3LYP/6-31G(d) calculations gave transition energies similar (the difference is mostly $<3\%$) to those obtained with the TD DFT B3LYP/6-31G(d) calculations (see Tables S8–S11 in the Supporting Information). The calculated

Table 3. Calculated energy levels of the excited states and their orbital contribution for compounds **1**-BF_2 and M**1**-BF_2 by using TD DFT B3LYP/6-31G(d) calculations in dichloromethane.

State	Energy [eV] (λ [nm])	Oscillator strength	Orbital (contribution)
1-BF_2			
1	2.247 (551.8)	2.277	H→L (0.70678)
2	2.752 (450.6)	0.072	H−1→L (0.69487)
			H→L+1 (0.13172)
3	3.677 (337.2)	0.299	H−2→L (0.61173)
			H−1→L+1 (−0.34603)
4	3.722 (333.1)	0.093	H−1→L (−0.13197)
			H→L+1 (0.69131)
M**1**-BF_2			
1	2.731 (454.1)	1.395	H→L (0.70835)
2	3.981 (311.5)	0.227	H−1→L (0.66848)
			H→L+1 (0.20553)
3	4.062 (305.2)	0.001	H−2→L (0.66598)
			H→L+2 (0.19600)
4	4.522 (274.2)	0.064	H−3→L (0.11504)
			H−2→L (0.19929)
			H→L+1 (0.46150)
			H→L+2 (−0.45531)

spectrum of compound **1**-BF_2in dichloromethane (Figure 6a), by using the polarizable continuum model (PCM), mimics rather well the experimental spectrum except that the energy of the band (especially the "cyanine-like" one) is blue shifted (see above), an expected trend with TD-DFT calculations.[36] The calculated TPA spectrum clearly shows that only the S_0–S_2 transition is active in the window $\lambda = 700$-1200 nm. For M**1**-BF_2, the one-photon absorption spectrum matches the TPA spectrum well (Figure 6b) as already shown in the experimental spectra.

To investigate the rotamer contribution of compounds **1**-BF_2 and M**1**-BF_2 to the TPA spectra, calculations were performed for those conformers in which the dioxaborine C–O bond and the C=C double bond experience an *s-trans* or *s-cis* relationship around the formally single C–C bond. The *s-trans s-trans*, *s-trans s-cis*, and *s-cis s-cis* isomers were considered (Figure S31 and S32 in the Supporting Information). The calculated spectra of the curcuminoid and hemicurcuminoid structures present similar features with only a decrease of the TP cross section values upon passing from the *s-trans* to a *s-cis* conformation. For those *s-cis* species of lower symmetry, one notes a slight increase of the TP-forbidden component (see above TPEF experiments) corresponding to an increase of the population of the S_1 excited state (Figure S31 in the Supporting Information, compare with the tenfold magnification of the TPA spectrum in Figure 6a).

Cell imaging

Cell imaging was performed by using three strategies. The first one involved compound **7**-BF_2. Owing to the presence of two hydrophilic chains, this compound is hydro-soluble and was incubated directly with Cos7 cells in an aqueous solution. The dye entered the cells and both one-photon excited fluorescence and TPEF revealed that uptake of the dye occurred

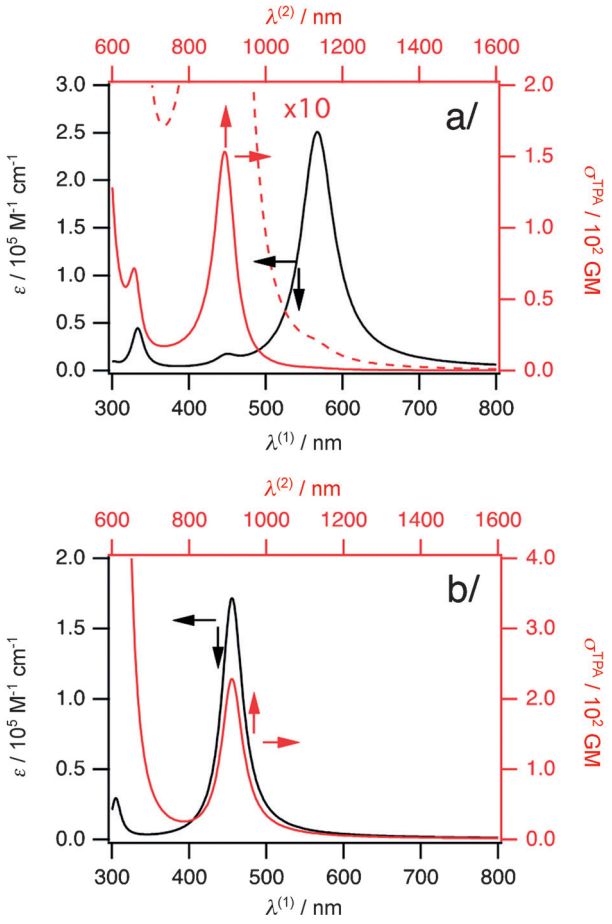

Figure 6. Simulated one-photon absorption (black line, bottom and left axes) and two-photon absorption (red solid line, top and right axes) spectra of compounds: a) **1**-BF_2, and b) M**1**-BF_2 in dichloromethane. The two-photon absorption spectrum of compound **1**-BF_2 with tenfold magnification for the right axis is also shown as the red dashed line. A Lorentzian function with a relaxation constant of 0.1 eV was used as line shape function.

within the cytoplasm. Introduction of compound **7**-BF_2 into the culture medium did not impede the reproduction of the Cos7 cells, and we did not notice any dead cells floating in the sample over 48 h, suggesting little to no toxicity for this dye. In this case, fluorescence emission was detected in the visible, out of the biological transparency window.

In order to implement a NIR-to-NIR approach, we used a previously published procedure to produce fluorescent organic particles by using hydrophobic dyes and showed that the solid-state emission was red shifted as compared to that in solution. To this end, we used the dyes **3**-BF_2 and **4**-BF_2, which provide high TPA brightness and far red to NIR emission already in solution. Upon addition of a low volume of a concentrated solution of these dyes (i.e., 30 μL, 10^{-4} M in THF) into water (3 mL), particles of various sizes were formed.[14] DLS measurements revealed that compound **4**-BF_2 forms large particles with diameters of approximately (622 ± 61) nm, whereas compound **3**-BF_2 forms particles with diameters of 265 nm. Notably, particles of both compounds were not emissive, which was attributed to the aggregation-induced quenching effect. Still, we performed incubation for 2 h of the particles in the

presence of Cos7 cells. The solution was then removed and the cells were washed three times with phosphate buffered saline (PBS) prior to imaging by using one- and TP microscopy. As depicted in Figure S34 in the Supporting Information, the Cos7 cells became fluorescently labeled upon exposure to particles of compounds **3**-BF_2, and**4**-BF_2. Because these aggregates are non-fluorescent and have sizes that are as big as those of the cells, we attributed the fluorescence enhancement to the penetration of compounds **3**-BF_2 and **4**-BF_2 as non-aggregated species due to a disaggregation mechanism at the cell membrane.[40] However, the spectra of the dyes within the cells resemble those obtained in the apolar dibutyl ether solvent with an emission in the visible region ($\lambda_{em} = 629$ nm, Figure S35 in the Supporting Information). We determined the TP brightness of compounds **3**-BF_2 and **4**-BF_2 (Figures S36 and S37 in the Supporting Information) in dibutyl ether. The values of 400 and 665 GM found for compounds **3**-BF_2 and **4**-BF_2, respectively, were thus lower than in dichloromethane. Such dependence of the TPA cross section of polar molecules have been recently discussed by Gryko et al.[41] Although the whole cell was labeled with compound **4**-BF_2, which prevented distinguishing the nuclei from the cell cytoplasm (Figure S34b in the Supporting Information), compound **3**-BF_2 did not enter the nuclei (Figure S34a in the Supporting Information), similarly to compound **7**-BF_2 (Figure S33 in the Supporting Information), allowing the visualization of the cell and its nucleus (by contrast) with both compounds **3**-BF_2 and **7**-BF_2.

These results by using pre-formed particles of compounds **3**-BF_2 and **4**-BF_2 show that the particles are disrupted at the cell membrane, leading to the uptake of non-aggregated dye molecules.[40] As such, we present a means of cell labeling with molecular fluorophores that are not water soluble. However, despite the uptake and imaging success of such method, disaggregation of the particles prevents NIR-to-NIR because the emission of curcuminoid borodifluoride molecules is located in the visible part of the spectrum.

In a third approach, the use of porous silica nanoparticles (PSNPs) as a vehicle for the cellular incorporation of compound **4**-BF_2 was attempted with the intent to preserve the NIR fluorescence emission of the dye. This strategy was adopted in order to improve the intracellular uptake and the in vivo imaging potential of these boron difluoride curcuminoid compounds by taking benefits from the NIR emission that could be due to the emission in the polar environment of silica. The large and easily accessible pores of the PSNPs, as well as their high endocytosis rate and low toxicity in mammalian cells render them ideal nanovessels.[42] After the synthetic preparation following well-established procedures,[43] transmission electron microscopy (TEM) was used to confirm the distribution of the particle sizes between 80 and 120 nm, with hexagonally arranged pores of about 2.2 nm in diameter.[43] Particles were loaded with a dye through soaking in saturated solutions (toluene) of compound **4**-BF_2 or fluorescein isothiocyanate (FITC), the latter dye being used for control experiments.

Interestingly, upon loading the PSPNs with compound **4**-BF_2, the fluorescence spectrum, when exciting at $\lambda = 560$ nm, presents a broad emission with its maximum at $\lambda = 650$ nm (Figure S38 in the Supporting Information). Although this value is close to that obtained in diethyl ether, the emission profile in the PSPNs is broader. Accordingly, upon exciting at $\lambda = 600$ nm, two broad peaks can be seen that are shifted to the red compared to the maximum previously observed (Figure S38 in the Supporting Information). This could therefore be attributed to the formation of small-size aggregates of compound **4**-BF_2, which have now a large part of their emission in the NIR region. Here, it must be noted that the fluorescence quantum yield is lower than in solution (10% when exciting at $\lambda =$ 560 nm) and this is consistent with the absence of emission in the particles where extensive aggregation takes place.

Confocal microscopy was then performed in human PANC-1 (pancreatic carcinoma) and BT-549 (mammary ductal carcinoma) cells, following exposure to 200 $\mu g\,mL^{-1}$ FITC-labeled (Figure S39 in the Supporting Information) or**4**-BF_2-labeled (Figure 7) or unlabeled PSNPs (Figure S39 in the Supporting Information). FITC was used as the reference fluorophore. Subsequent to incubation of compound **4**-BF_2 and wash cycles, the cells were then supplemented with the anthraquinone-based DNA-detecting dye DRAQ5, which is known to allow for specific nucleus visualization. We observed that the PSNPs were taken up in the cells and accumulate in the cytoplasm but did not enter the nucleus according to the emission detected in the orange–red part of the spectrum (Figure 7, panels C, D, G, and H). The nuclei exhibited only the far-red fluorescence characteristic of DRAQ5 (Figure 7, panels B, D, F, and H). As compared to the previous case of the neat **4**-BF_2 nanoparticles that were disrupted when entering the cell, the porous silica nanoparticles offer a protecting shell to the small aggregates of **4**-BF_2 molecules, which preserves fluorescence emission and enables imaging in a wavelength range reaching the NIR region.

Conclusions

We have reported the synthesis of a series of new curcuminoid boron difluoride complexes that absorb far in the visible and emit up to the NIR region of the spectrum. Such properties have been obtained by increasing the strength of the end-donor group and by rigidifying the structure of the backbone or of the donor moiety. The free ligands and their boron difluoride complexes exhibit a similar optical trends, boron difluoride complexation causes a dramatic increase in the acceptor strength, which in turn results in enhanced linear and non-linear optical properties. We show that those complexes exhibit efficient TPEF with TPA ranging from the visible to the NIR region (up to $\lambda = 990$ nm), high TPA cross section (up to ≈ 5000 GM), and brightness (i.e., 400–900 GM. By using a combination of experimental TPEF and Z-scan measurements and a TD-DFT study, we evidenced that the TPA process involves the S_0–S_2 transition. Hemicurcuminoid ligands and their corresponding boron difluoride complexes served as dipolar model species and provided useful insights into the understanding of the photophysics of the curcuminoid compounds. In summary, the modular synthetic approach allows a rational tuning of the curcuminoid chemical and electronic structure, which leads to dyes with versatile optical properties useful for cell imaging.

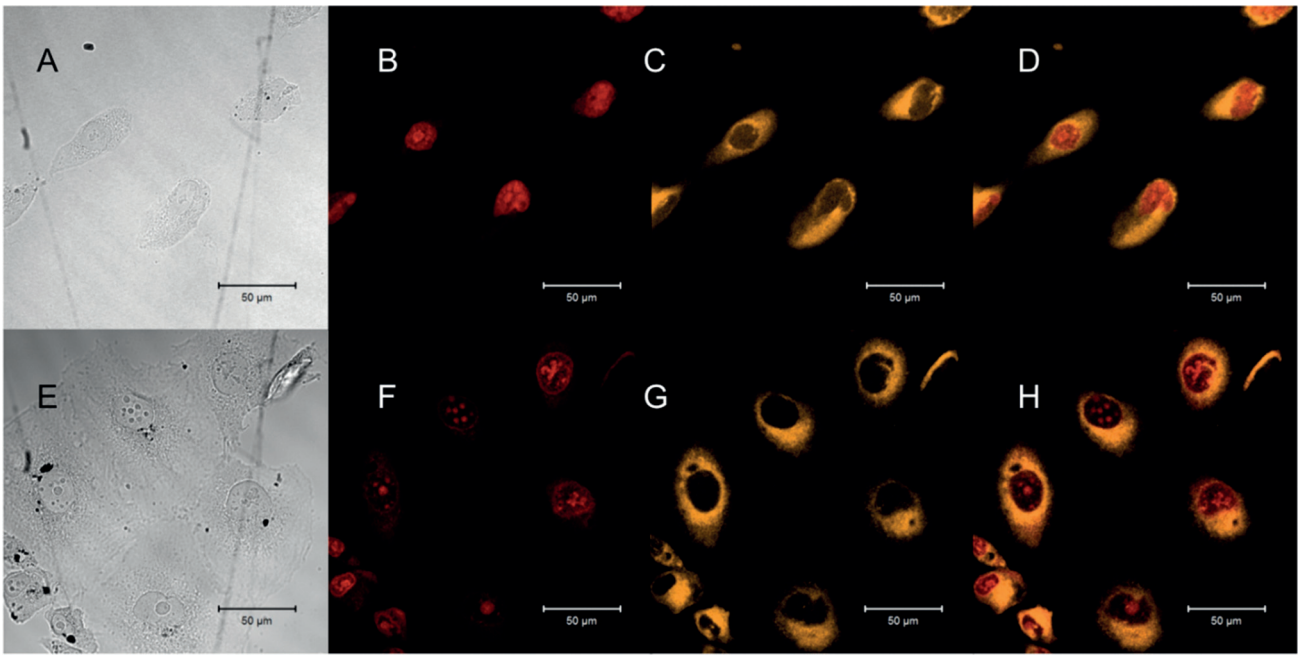

Figure 7. Confocal images of human BT-549 (top) and PANC-1 (bottom) cells, following exposure to 200 μg mL^{-1} **4**-BF_2-labeled porous silica nanoparticles and then to the DRAQ5 dye. A, E) Bright-field/DIC (T-PMT). B, F) Luminescence of DRAQ5 recorded selectively at $\lambda_{exc}=633/\lambda_{em}=691–758$ nm. C, G) Luminescence of compound **4**-BF_2 recorded selectively at $\lambda_{exc}=458/\lambda_{em}=625–675$ nm. D, H) Superimposition of panels B and C and F and H, respectively.

Accordingly, we successfully tagged Cos7, PANC-1, and BT-549 cells by implementing three different uptake strategies that all take benefit of the key optical attributes of the boron difluoride complexes of curcuminoid chromophores.

Experimental Section

Materials and instrumentation

All solvents for synthesis were of analytic grade. Spectroscopy measurements were carried out with spectroscopic grade solvents. NMR spectra (^{1}H, ^{13}C, and ^{19}F) were recorded at room temperature on a BRUKER AC 250 spectrometer operating at 250, 62.5, and 235 MHz for ^{1}H, ^{13}C, and ^{19}F, respectively. Data are listed in parts per million (ppm) and are reported relative to tetramethylsilane (^{1}H and ^{13}C); residual solvent peaks of the deuterated solvents were used as internal standard. Mass spectra were obtained in Spectropole, Marseille (http://www.spectropole.fr/). Spectroscopic measurements and X-ray structure determinations were performed according to published methodologies.[19b] Compounds **1**-H, **1**-BF_2,[13a] **2**-H,[44] **6**-H,[45] **5**-BF_2,[12] **8**-BF_2,[13d] M**1**-H, M**6**-H, M**1**-BF_2, and M**6**-BF_2[46] were synthesized following published procedures.

Z-scan measurements

A femtosecond optical parametric amplifier (SpectraPhysics OPA-800, pumped by a regenerative amplifier, Spitfire) was used as the light source for the Z-scan measurements. The repetition rate and the pulse width were 1 kHz and 120–140 fs full width at half maximum (FWHM), respectively, depending on the wavelength. The sample solution was hold in 2 mm quartz cuvette, which is much shorter than the Rayleigh range of the optical setup (6–8 mm) and satisfies the thin-sample condition for the analysis. The concentrations of the sample solutions were 0.64–1.1 mM for compound **3**-BF_2, 0.38–0.41 mM for compound **4**-BF_2, and 2.0 mM for compound M**1**-BF_2 (all in spectroscopic grade dichloromethane). At least 400 shots of laser pulses whose fluctuation was smaller than 5% were averaged to obtain data points of each sample position of the Z-scan traces. Analysis of open-aperture Z-scan trace was performed by curve fitting of the theoretical equation that assumes spatial and temporal Gaussian pulses.[27b] The incident power (i.e., the average power) was varied in the range of 0.005–0.4 mW. The corresponding on-axis peak intensities were below 150 GW cm^{-2}. Typical open-aperture Z-scan traces are presented in the Supporting Information (Figures S40, S42, and S44). For compounds **3**-BF_2 and **4**-BF_2, deformed traces (flatten bottom, Figures S41 and S43 in the Supporting Information) the mean saturation of TPA[47] were observed at the incident power over 0.07 mW. Thus, these deformed traces were excluded for the analysis. The linear relation between the on-axis TP absorbance q_0 obtained by the curve fit to the observed traces against the incident power was confirmed (Figures S40, S42, and S44 in the Supporting Information) as the criteria that the observed Z-scan signal, that is, the depression of the transmittance near the focal point, originates from the TPA process. The TP coefficient β was obtained from the slope of the plots. The TPA cross section was obtained by using the convention, $\sigma^{TPA}=h\nu\beta/N$, where $h\nu$ is the photon energy and N is the number density. A solution of rhodamine in methanol (6.5 mM) was measured at the same time for $\lambda=950–1160$ nm and the obtained TPA cross section was close to the reported value (for example, $\sigma^{TPA}=(41\pm6)$ GM was obtained at λ1024 nm and the reported value was 35 GM.[28]

Simulation of the one- and two-photon absorption spectra

All molecular orbital calculations were performed with the Gaussian 09 program package.[48] The geometries of the model molecules (i.e., compounds **1**-BF_2 and M**1**-BF_2) were optimized at the B3LYP/6–31(d) level. The optimized geometries are presented in Table S12

in the Supporting Information. Then TD-B3LYP/6–31G(d) calculations were performed on the optimized geometry. To calculate the transition dipole moments between the excited states, the Tamm–Dancoff approximation (TDA) was adapted for the TD-DFT calculations (KEYWORD "tda(allTransitionDensities)"; revision D01 is necessary to run this keyword). The ground state-to-excited state dipole moments, the permanent dipole moment in the ground state, and the excitation energies were also obtained from the TD-B3LYP/6–31G(d) calculations; nevertheless, the results of the TDA-B3LYP/6–31G(d) calculations were used for consistency, to simulate the spectrum. The permanent dipole moments in the *i*th excited states were calculated by repeating the TDA-B3LYP/6–31G(d) calculations with the KEYWORD "tda(root = *i*)" for $i = 1 \ldots N$. For all TD-DFT calculations, the lowest twenty excited states ($N = 20$) were calculated, and then considered for the simulation. The sum-over-state formulation used for the spectral simulation were reported previously.[38] The relaxation constant of the Lorenzian linewidth function was taken to be 0.10 eV for both the one- and two-photon absorptions. All calculations were performed in vacuum and in dichloromethane ($\varepsilon = 8.93$) with the PCM[49] (Figures S31 and S32 and Tables S8–S11 in the Supporting Information).

Synthesis and loading of the nanoparticles

The porous silica nanoparticles (PSNPs, MCM-41) were prepared according to a previously described procedure[43] and stored in a methanol suspension until use, and the particle quality was confirmed through TEM measurements acquired on a JEOL 2100-F analytical transmission electron microscope. The particles (2.6 mg) were centrifuged (12000 rpm, 5 min) and re-suspended three times in toluene (2 mL). Following the final wash cycle, the particles were re-suspended in a final volume of 1 mL toluene, and an aliquot (330 μL, 0.6 mg) was added to a toluene solution of compound **4**-BF_2 (1 mL, 188 μg mL^{-1}) in a scintillation vial. The samples were stirred overnight, while shielded from light to mitigate any possible photobleaching effects. The nanoparticles were then washed four times through repeated cycles of centrifugation and re-suspension in fresh toluene as specified above. Following this treatment, the silica particles acquire a dark blue color, as a result of the incorporation of compound **4**-BF_2. The particles were then re-suspended in toluene to a final concentration of approximately 0.6 mg mL^{-1} just prior to spectral acquisition. The silica particles modified with FITC (Sigma–Aldrich) were prepped in a similar manner to that of the **4**-BF_2 samples, with saturated dye suspension and wash steps being performed in ethanol instead of toluene. The labeled nanoparticles were re-suspended in cell culture media prior to conducting the cellular studies.

Cell culture

The cos-7 cells were grown in Dulbecco's modified Eagle's medium (DMEM) with 10% fetal calf serum, 1% L-glutamine, 1% penicillin/streptomycin) and 1% pyruvate. For imaging, the cells were cultured in 6-well tissue culture glass slides.

Two human cell lines were used to follow the cellular uptake of the dye-loaded nanoparticles. Human pancreatic carcinoma cells (PANC-1, ATCC) were grown in DMEM (BioWhittaker, Walkersville, MD) supplemented with 10% fetal bovine serum (ATCC), and human mammary ductal carcinoma cells (BT-549, ATCC) were grown in RPMI-1640 (Life Technologies, Grand Island, NY) supplemented with 10% fetal bovine serum and 0.023 IU mL^{-1} insulin (Life Technologies). The cell cultures were maintained in a humidified atmosphere at 37 °C in 5% CO_2/95% air. The cells were subcultured by rinsing once with trypsin-versene (BioWhittaker) and incubating at room temperature with additional trypsin-versene for 5 min or until the cells detached. Cells were then gently re-suspended in fresh medium and aliquoted into flasks.

Cell treatment and imaging

Cells were seeded at 50000 cells per well (100 μL per well) in 8-well chamber slides (Nunc™ Lab-Tek™ Chambered Coverglass™ System, Thermo Scientific). At 24 h post-seeding, a loaded-nanoparticle suspension (150 μL per well, final concentration 0.2 mg mL^{-1}) was added to each well of the chamber slide. At 48 h post-seeding, the medium was removed and the wells were washed twice with DPBS (Life Technologies). The wells were supplemented with 4% paraformaldehyde (150 μL per well, Alfa Aesar), followed by incubation at room temperature for 10 min. The wells were then washed thrice with DPBS, supplemented with DRAQ5 (0.1 μmol L^{-1} in PBS, 125 μL per well, Thermo Scientific), and incubated at room temperature for 20 min. Finally, the wells were washed again thrice with DPBS, supplemented with DPBS (200 μL per well), covered with foil and stored at 4 °C. Slides were brought to room temperature 2 h prior to image collection on a Zeiss LSM 710 confocal microscope. Images were taken by using water and a magnification of 40× and processed with ZEN 2012 SP1 (black edition, 64 bit, Release Version 8.1, Carl Zeiss Microscopy)

Synthesis

The curcuminoid derivatives were synthesized as described elsewhere[12] except for compound **2**-BF_2 that was prepared as follows: In a 50 mL flask, 2-acetylcyclohexanone (1.40 g, 10 mmol), 4-(*N*-dimethyl)aminobenzaldehyde (2.98 g, 20 mmol), boric acid (696 mg, 10 mmol), morpholine (50 mg, 0.57 mmol), and acetic acid (50 mg, 0.83 mmol) were mixed in the absence of solvent. The sample was irradiated for 2 min at 200 °C and atmospheric pressure in a microwave reactor. After cooling to room temperature, the resulting solid was sonicated for 1 h in ethyl acetate and filtered through a glass filter. The ligand **2**-H was then mixed with boron trifluoride etherate (1.1 equiv) in dichloromethane and stirred while heating to reflux for 16 h. After reducing the volume of the solvent, the residue was filtered on a flash-chromatography column with silica gel, by using dichloromethane as the eluent.

***2*-BF_2**: ^{1}H NMR ($CDCl_3$, 250 MHz): $\delta = 7.89$ (d, $^3J = 15.0$ Hz, 1H), 7.83–7.80 (m, 3H), 7.52 (d, $^3J = 9.0$ Hz, 2H), 6.98 (d, $^3J = 15.0$ Hz, 1H), 6.79 (d, $^3J = 8.7$ Hz, 2H), 6.78 (d, $^3J = 9.0$ Hz, 2H), 3.07 (s, 3H), 3.03 (s, 3H), 2.79 (t, $^3J = 5.5$ Hz, 2H), 2.67 (t, $^3J = 5.3$ Hz, 2H), 1.76–1.72 ppm (m, 2H); ^{19}F NMR ($CDCl_3$, 235 MHz): $\delta = -140.50$ (^{10}B, 0.2F), −140.56 ppm (^{10}B, 0.8F); ^{13}C NMR ($CDCl_3$, 62.5 MHz): Because of the poor solubility of **2**-BF_2, a satisfactory ^{13}C NMR spectrum could not be obtained. HRMS (ESI+): *m/z* calcd for $C_{26}H_{29}N_2O_2F_2BNa^+$: 473.2187 $[M+Na]^+$; found: 473.2188.

***3*-H**: ^{1}H NMR ($CDCl_3$, 250 MHz): $\delta = 7.86$ (d, $^3J = 15.8$ Hz, 2H), 7.39 (d, $^3J = 9.0$ Hz, 2H), 6.57 (d, $^3J = 15.8$ Hz, 2H), 6.27 (dd, $^3J = 8.8$, $^4J = 2.5$ Hz, 2H), 6.12 (d, $^4J = 2.3$ Hz, 2H), 5.68 (s, 1H), 3.99 (t, $^3J = 6.5$ Hz, 4H), 3.39 (q, $^3J = 7.0$ Hz, 8H), 1.96–1.84 (m, 4H), 1.20 (t, $^3J = 7.0$ Hz, 12H), 1.11 ppm (t, $^3J = 7.5$ Hz, 6H); ^{13}C NMR ($CDCl_3$, 62.5 MHz): $\delta =$ 183.73, 159.95, 150.44, 135.91, 130.72, 119.39, 112.32, 104.42, 100.48, 95.01, 69.76, 44.56, 22.63, 12.69, 10.77 ppm; HRMS (ESI+): *m/z* calcd for $C_{33}H_{46}N_2O_4H^+$: 535.3530 $[M+Na]^+$; found: 535.3529.

***3*-BF_2**: ^{1}H NMR ($CDCl_3$, 250 MHz): $\delta = 8.13$ (d, $^3J = 15.3$ Hz, 2H), 7.38 (d, $^3J = 9.0$ Hz, 2H), 6.65 (d, $^3J = 15.5$ Hz, 2H), 6.28 (dd, $^3J = 9.0$, $^4J = 2.0$ Hz, 2H), 6.08 (d, $^4J = 1.5$ Hz, 2H), 5.79 (s, 1H), 4.00 (t, $^3J = 6.5$ Hz, 4H), 3.42 (q, $^3J = 7.0$ Hz, 8H), 1.96–1.88 (m, 4H), 1.22 (t, $^3J = 7.0$ Hz,

12H), 1.11 ppm (d, $^3J=7.5$ Hz, 6H); ^{19}F NMR ($CDCl_3$, 235 MHz): $\delta=-141.41$ (^{10}B, 0.2F), -141.47 ppm (^{11}B, 0.8F); ^{13}C NMR ($CDCl_3$, 62.5 MHz): $\delta=177.62$, 161.32, 151.84, 142.06, 132.86, 115.38, 115.28, 104.84, 100.57, 94.42, 69.81, 44.79, 22.54, 12.71, 10.76 ppm; HRMS (ESI+): *m/z* calcd for $C_{33}H_{45}N_2O_4F_2BNa^+$: 605.3339 $[M+Na]^+$; found: 605.3337.

4-H: ^{1}H NMR ($CDCl_3$, 250 MHz): $\delta=7.80$ (d, $^3J=16.0$ Hz, 2H), 7.07 (s, 2H), 6.43 (d, $^3J=15.8$ Hz, 2H), 5.69 (s, 1H), 3.73 (t, $^3J=6.5$ Hz, 4H), 3.23–3.18 (m, 8H), 2.74 (q, $^3J=6.5$ Hz, 8H), 1.98–1.81 (m, 12H), 1.09 ppm (t, $^3J=7.5$ Hz, 6H); ^{13}C NMR ($CDCl_3$, 62.5 MHz): $\delta=$ 183.52, 155.81, 145.52, 153.87, 125.96, 119.33, 117.32, 115.63, 113.96, 100.28, 75.63, 49.45, 49.66, 27.52, 23.57, 21.83, 21.52, 21.30, 10.67 ppm; HRMS (ESI+): *m/z* calcd for $C_{37}H_{46}N_2O_4H^+$: 583.3530 $[M+Na]^+$; found: 583.3530.

4-BF$_2$: ^{1}H NMR ($CDCl_3$, 250 MHz): $\delta=8.08$ (d, $^3J=15.3$ Hz, 2H), 7.08 (s, 2H), 6.50 (d, $^3J=15.3$ Hz, 2H), 5.80 (s, 1H), 3.73 (t, $^3J=6.5$ Hz, 4H), 3.28–3.22 (m, 8H), 2.75–2.69 (m, 8H), 1.97–1.84 (m, 12H), 1.11 ppm (t, $^3J=7.5$ Hz, 2H); ^{19}F NMR ($CDCl_3$, 235 MHz): $\delta=-142.95$ (^{10}B, 0.2F), -143.00 ppm (^{11}B, 0.8F); ^{13}C NMR ($CDCl_3$, 62.5 MHz): $\delta=177.38$, 157.19, 147.16, 141.70, 127.48, 117.59, 115.23, 114.93, 113.92, 100.41, 75.88, 50.07, 49.77, 27.46, 23.53, 21.55, 20.99, 10.63 ppm; HRMS (ESI+): *m/z* calcd for $C_{37}H_{45}N_2O_4F_2BK^+$: 669.3079 $[M+K]^+$; found: 669.3081.

6-BF$_2$: ^{1}H NMR ([D$_6$]DMSO, 250 MHz): $\delta=8.00$ (d, $^3J=15.8$ Hz, 2H), 7.81 (d, $^3J=8.3$ Hz, 4H), 7.36 (d, $^3J=8.3$ Hz, 4H), 7.18 (d, $^3J=$ 15.8 Hz, 2H), 6.59 (s, 1H), 2.55 ppm (s, 6H); ^{19}F NMR ($CDCl_3$, 235 MHz): $\delta=-140.76$ (^{10}B, 0.2F), -140.82 ppm (^{11}B, 0.8F); ^{13}C NMR ([D$_6$]DMSO, 62.5 MHz): $\delta=179.31$, 146.08, 144.29, 130.29, 129.84, 125.45, 120.00, 101.96, 13.90 ppm; HRMS (ESI+): *m/z* calcd for $C_{21}H_{19}O_2S_2F_2BK^+$: 455.0523 $[M+K]^+$; found: 455.0520.

7-H: ^{1}H NMR ($CDCl_3$, 250 MHz): $\delta=7.59$ (d, $^3J=15.8$ Hz, 2H), 7.47 (d, $^3J=8.5$ Hz, 4H), 6.91 (d, $^3J=8.5$ Hz, 4H), 6.47 (d, $^3J=15.8$ Hz, 2H), 5.76 (s, 1H), 4.16 (t, $^3J=4.8$ Hz, 4H), 3.86 (t, $^3J=4.8$ Hz, 4H), 3.71–3.69 (m, 4H), 3.59–3.55 (m, 4H), 3.38 ppm (s, 6H); ^{13}C NMR ($CDCl_3$, 62.5 MHz): $\delta=183.26$, 160.44, 140.01, 129.66, 127.90, 121.84, 114.97, 101.28, 71.89, 70.73, 69.57, 67.48, 59.00 ppm; HRMS (ESI+): *m/z* calcd for $C_{29}H_{36}O_8H^+$: 513.2483 $[M+Na]^+$; found: 513.2482.

7-BF$_2$: ^{1}H NMR ([D$_6$]DMSO, 250 MHz): $\delta=7.98$ (d, $^3J=15.5$ Hz, 2H), 7.84 (d, $^3J=8.5$ Hz, 4H), 7.09–7.03 (m, 6H), 6.51 (s, 1H), 4.20 (d, $^3J=$ 4.8 Hz, 4H), 3.76 (d, $^3J=4.0$ Hz, 4H), 3.61–3.58 (m, 4H), 3.48–3.44 (m, 4H), 3.25 ppm (s, 6H); ^{19}F NMR ([D$_6$]DMSO, 235 MHz): $\delta=$ -137.80 (^{10}B, 0.2F), -137.86 ppm (^{11}B, 0.8F); ^{13}C NMR ([D$_6$]DMSO, 62.5 MHz): $\delta=179.08$, 161.71, 146.22, 131.62, 126.83, 118.67, 115.18, 101.48, 71.16, 69,61, 68.63, 67.47, 57.95 ppm; HRMS (ESI+): *m/z* calcd for $C_{29}H_{35}O_8F_2BK^+$: 599.2030 $[M+K]^+$; found: 599.2037.

Acknowledgements

A.D. and F.F. would like to thank the Spectropole de Marseille and, especially, C. Chendo and V. Monnier for performing the mass spectrometry analysis and M. Giorgi for providing the X-ray crystallography. D.J. acknowledges the European Research Council (ERC) and the Région des Pays de la Loire for financial support in the framework of a Starting Grant (Marches - 278845) and the LumoMat Project, respectively. This research used resources of: 1) the GENCI-CINES/IDRIS, 2) the CCIPL (Centre de Calcul Intensif des Pays de Loire), 3) a local Troy cluster, and 4) a Grant-in-Aid for Scientific Research #25248007 (K.K.) from JSPS and #15H00966 (K.K., Innovative Areas "Stimuli-Responsive Chemical Species") from MEXT, Japan. This work was performed by using the France-BioImaging infrastructure supported by the Agence Nationale de la Recherche (ANR-10-INSB-04-01). R.J.A. acknowledges support from the US Department of Energy, Office of Science, Office of Basic Energy Sciences, Chemical Sciences, Geosciences, and Biosciences Division at the Lawrence Berkeley National Laboratory under Contract DE-AC02-05CH11231, through an Early Career Award. K.K. thanks Dr. Koji Ohta, Kyoto University, for his helpful suggestions on the quantum chemical calculations. M.P.-V. thanks the ANR (project ANR-14-CE05-0035-02) for his postdoctoral grant.

Keywords: cell imaging · density functional calculations · dipolar dyes · photophysics · two-photon processes

[1] a) X. Wang, A. R. Morales, T. Urakami, L. Zhang, M. V. Bondar, M. Komatsu, K. D. Belfield, *Bioconjugate Chem.* **2011**, *22*, 1438–1450; b) E. De Meulenaere, W.-Q. Chen, S. Van Cleuvenbergen, M.-L. Zheng, S. Psilodimitrakopoulos, R. Paesen, J.-M. Taymans, M. Ameloot, J. Vanderleyden, P. Loza-Alvarez, X.-M. Duan, K. Clays, *Chem. Sci.* **2012**, *3*, 984–995; c) X. J. Feng, P. L. Wu, F. Bolze, H. W. C. Leung, K. F. Li, N. K. Mak, D. W. J. Kwong, J.-F. Nicoud, K. W. Cheah, M. S. Wong, *Org. Lett.* **2010**, *12*, 2194–2197; d) C. Andraud, O. Maury, *Eur. J. Inorg. Chem.* **2009**, 4343–4343.

[2] a) D. Gao, R. R. Agayan, H. Xu, M. A. Philbert, R. Kopelman, *Nano Lett.* **2006**, *6*, 2383–2386; b) J. Arnbjerg, A. Jiménez-Banzo, M. J. Paterson, S. Nonell, J. Borrell, O. Christiansen, P. R. Ogilby, *J. Am. Chem. Soc.* **2007**, *129*, 5188–5199; c) S. Kim, T. Y. Ohulchanskyy, H. E. Pudavar, R. K. Pandey, P. N. Prasad, *J. Am. Chem. Soc.* **2007**, *129*, 2669–2675; d) T. Gallavardin, M. Maurin, S. Marotte, T. Simon, A.-M. Gabudean, Y. Bretonniere, M. Lindgren, F. Lerouge, P. L. Baldeck, O. Stephan, Y. Leverrier, J. Marvel, S. Parola, O. Maury, C. Andraud, *Photochem. Photobiol. Sci.* **2011**, *10*, 1216–1225.

[3] a) D. J. Bharali, D. W. Lucey, H. Jayakumar, H. E. Pudavar, P. N. Prasad, *J. Am. Chem. Soc.* **2005**, *127*, 11364–11371; b) Q. Lin, Q. Huang, C. Li, C. Bao, Z. Liu, F. Li, L. Zhu, *J. Am. Chem. Soc.* **2010**, *132*, 10645–10647.

[4] a) K.-S. Lee, D.-Y. Yang, S. H. Park, R. H. Kim, *Polym. Adv. Technol.* **2006**, *17*, 72–82; b) W. Zhou, S. M. Kuebler, K. L. Braun, T. Yu, J. K. Cammack, C. K. Ober, J. W. Perry, S. R. Marder, *Science* **2002**, *296*, 1106–1109; c) B. H. Cumpston, S. P. Ananthavel, S. Barlow, D. L. Dyer, J. E. Ehrlich, L. L. Erskine, A. A. Heikal, S. M. Kuebler, I. Y. S. Lee, D. McCord-Maughon, J. Qin, H. Rockel, M. Rumi, X.-L. Wu, S. R. Marder, J. W. Perry, *Nature* **1999**, *398*, 51–54; d) A. Ovsianikov, J. Viertl, B. Chichkov, M. Oubaha, B. MacCraith, I. Sakellari, A. Giakoumaki, D. Gray, M. Vamvakaki, M. Farsari, C. Fotakis, *ACS Nano* **2008**, *2*, 2257–2262.

[5] a) G. S. He, B. A. Reinhardt, J. C. Bhatt, A. G. Dillard, G. C. Xu, P. N. Prasad, *Opt. Lett.* **1995**, *20*, 435–437; b) Y. Morel, A. Irimia, P. Najechalski, Y. Kervella, O. Stephan, P. L. Baldeck, C. Andraud, *J. Chem. Phys.* **2001**, *114*, 5391–5396; c) P.-A. Bouit, K. Kamada, P. Feneyrou, G. Berginc, L. Toupet, O. Maury, C. Andraud, *Adv. Mater.* **2009**, *21*, 1151–1154; d) Q. Bellier, N. S. Makarov, P.-A. Bouit, S. Rigaut, K. Kamada, P. Feneyrou, G. Berginc, O. Maury, J. W. Perry, C. Andraud, *Phys. Chem. Chem. Phys.* **2012**, *14*, 15299–15307.

[6] a) D. A. Parthenopoulos, P. M. Rentzepis, *Science* **1989**, *245*, 843–845; b) H. E. Pudavar, M. P. Joshi, P. N. Prasad, B. A. Reinhardt, *Appl. Phys. Lett.* **1999**, *74*, 1338–1340.

[7] H. M. Kim, B. R. Cho, *Chem. Rev.* **2015**, *115*, 5014–5055.

[8] a) M. Albota, D. Beljonne, J.-L. Brédas, J. E. Ehrlich, J.-Y. Fu, A. A. Heikal, S. E. Hess, T. Kogej, M. D. Levin, S. R. Marder, D. McCord-Maughon, J. W. Perry, H. Röckel, M. Rumi, G. Subramaniam, W. W. Webb, X.-L. Wu, C. Xu, *Science* **1998**, *281*, 1653–1656; b) F. Terenziani, C. Katan, E. Badaeva, S. Tretiak, M. Blanchard-Desce, *Adv. Mater.* **2008**, *20*, 4641–4678; c) J. M. Hales, J. Matichak, S. Barlow, S. Ohira, K. Yesudas, J.-L. Brédas, J. W. Perry, S. R. Marder, *Science* **2010**, *327*, 1485–1488; d) O. V. Przhonska, S. Webster, L. A. Padilha, H. Hu, A. D. Kachkovski, D. J. Hagan, E. W. Van Stryland, in *Two-Photon Absorption in NIR-Conjugated Molecules: Design Strategy and Structure–Property Relations, Vol. 8, Springer Series on Fluorescence*, Springer, Heidelberg, **2010**, pp. 105–147; e) K. Matsui, Y.

Segawa, T. Namikawa, K. Kamada, K. Itami, *Chem. Sci.* **2013**, *4*, 84 – 88; f) K. Kamada, S.-I. Fuku-en, S. Minamide, K. Ohta, R. Kishi, M. Nakano, H. Matsuzaki, H. Okamoto, H. Higashikawa, K. Inoue, S. Kojima, Y. Yamamoto, *J. Am. Chem. Soc.* **2013**, *135*, 232 – 241.

[9] a) C. Xu, W. W. Webb, *J. Opt. Soc. Am. B* **1996**, *13*, 481 – 491; b) P. Didier, G. Ulrich, Y. Mely, R. Ziessel, *Org. Biomol. Chem.* **2009**, *7*, 3639 – 3642; c) Q. Zheng, G. Xu, P. N. Prasad, *Chem. Eur. J.* **2008**, *14*, 5812 – 5819; d) Q. Zheng, G. S. He, P. N. Prasad, *Chem. Phys. Lett.* **2009**, *475*, 250 – 255.

[10] H.-J. Li, W.-F. Fu, L. Li, X. Gan, W.-H. Mu, W.-Q. Chen, X.-M. Duan, H.-B. Song, *Org. Lett.* **2010**, *12*, 2924 – 2927.

[11] E. Cogné-Laage, J.-F. Allemand, O. Ruel, J.-B. Baudin, V. Croquette, M. Blanchard-Desce, L. Jullien, *Chem. Eur. J.* **2004**, *10*, 1445 – 1455.

[12] A. Felouat, A. D'Aléo, F. Fages, *J. Org. Chem.* **2013**, *78*, 4446 – 4455.

[13] a) C. Ran, X. Xu, S. B. Raymond, B. J. Ferrara, K. Neal, B. J. Bacskai, Z. Medarova, A. Moore, *J. Am. Chem. Soc.* **2009**, *131*, 15257 – 15261; b) X. Zhang, Y. Tian, Z. Li, X. Tian, H. Sun, H. Liu, A. Moore, C. Ran, *J. Am. Chem. Soc.* **2013**, *135*, 16397 – 16409; c) G. Bai, C. Yu, C. Cheng, E. Hao, Y. Wei, X. Mu, L. Jiao, *Org. Biomol. Chem.* **2014**, *12*, 1618; d) K. Liu, J. Chen, J. Chojnacki, S. Zhang, *Tetrahedron Lett.* **2013**, *54*, 2070 – 2073.

[14] A. D'Aléo, A. Felouat, V. Heresanu, A. Ranguis, D. Chaudanson, A. Karapetyan, M. Giorgi, F. Fages, *J. Mater. Chem. C* **2014**, *2*, 5208 – 5215.

[15] K. Rurack, M. L. Dekhtyar, J. L. Bricks, U. Resch-Genger, W. Rettig, *J. Phys. Chem. A* **1999**, *103*, 9626 – 9635.

[16] G. Görlitz, H. Hartmann, B. Nuber, J. J. Wolff, *J. Prakt. Chem.* **1999**, *341*, 167 – 172.

[17] C. E. Nichols, D. Youssef, R. G. Harris, A. Jha, *ARKIVOC (Gainesville, FL, U.S.)* **2006**, *13*, 64 – 72.

[18] CCDC 1051816 (**3**-H) and 1051817 (**4**-H) contain the supplementary crystallographic data for this paper. These data are provided free of charge by The Cambridge Crystallographic Data Centre.

[19] a) A. D'Aléo, D. Gachet, V. Heresanu, M. Giorgi, F. Fages, *Chem. Eur. J.* **2012**, *18*, 12764 – 12772; b) A. D'Aléo, V. Heresanu, M. Giorgi, B. Le Guennic, D. Jacquemin, F. Fages, *J. Phys. Chem. C* **2014**, *118*, 11906 – 11918.

[20] T. Teshima, M. Takeishi, T. Arai, *New J. Chem.* **2009**, *33*, 1393 – 1401.

[21] A. D'Aléo, F. Fages, *Photochem. Photobiol. Sci.* **2013**, *12*, 500 – 510.

[22] Z. R. Grabowski, K. Rotkiewicz, W. Rettig, *Chem. Rev.* **2003**, *103*, 3899 – 4031.

[23] J. Fabian, H. Hartmann, *J. Phys. Org. Chem.* **2004**, *17*, 359 – 369.

[24] F. Terenziani, A. Painelli, C. Katan, M. Charlot, M. Blanchard-Desce, *J. Am. Chem. Soc.* **2006**, *128*, 15742 – 15755.

[25] a) R. Englman, J. Jortner, *Mol. Phys.* **1970**, *18*, 145 – 164; b) B. R. Henry, W. Siebrand, in *Organic Molecular Photophysics, Vol. 1* (Ed.: J. B. Birks), Wiley, New York, **1973**.

[26] A. Bourdolle, M. Allali, A. D'Aléo, P. L. Baldeck, K. Kamada, J. A. G. Williams, H. Le Bozec, C. Andraud, O. Maury, *ChemPhysChem* **2013**, *14*, 3361 – 3367.

[27] a) M. Sheik-Bahae, A. A. Said, T. H. Wei, D. J. Hagan, E. W. Van Stryland, *IEEE J. Quantum Electron.* **1990**, *26*, 760 – 769; b) K. Kamada, K. Matsunaga, A. Yoshino, K. Ohta, *J. Opt. Soc. Am. B* **2003**, *20*, 529 – 537.

[28] N. S. Makarov, M. Drobizhev, A. Rebane, *Opt. Express* **2008**, *16*, 4029 – 4049.

[29] M. Drobizhev, N. S. Makarov, Y. Stepanenko, A. Rebane, *J. Chem. Phys.* **2006**, *124*, 224701/224701 – 224701/224711.

[30] M. Rumi, J. E. Ehrlich, A. A. Heikal, J. W. Perry, S. Barlow, Z. Hu, D. McCord-Maughon, T. C. Parker, H. Röckel, S. Thayumanavan, S. R. Marder, D. Beljonne, J.-L. Brédas, *J. Am. Chem. Soc.* **2000**, *122*, 9500 – 9510.

[31] K. Kamada, Y. Iwase, K. Sakai, K. Kondo, K. Ohta, *J. Phys. Chem. C* **2009**, *113*, 11469 – 11474.

[32] J. A. Tiburcio-Moreno, J. J. Alvarado-Gil, C. Diaz, L. Echevarria, F. E. Hernández, *Chem. Phys. Lett.* **2013**, *583*, 160 – 164.

[33] a) H. Hu, O. V. Przhonska, F. Terenziani, A. Painelli, D. Fishman, T. R. Ensley, M. Reichert, S. Webster, J. L. Bricks, A. D. Kachkovski, D. J. Hagan, E. W. Van Stryland, *Phys. Chem. Chem. Phys.* **2013**, *15*, 7666 – 7678; b) W. M. McClain, *Acc. Chem. Res.* **1974**, *7*, 129 – 135.

[34] A. D'Aléo, A. Picot, P. L. Baldeck, C. Andraud, O. Maury, *Inorg. Chem.* **2008**, *47*, 10269 – 10279.

[35] a) A. D. Becke, *J. Chem. Phys.* **1993**, *98*, 5648 – 5652; b) P. J. Stephens, F. J. Devlin, C. F. Chabalowski, M. J. Frisch, *J. Phys. Chem.* **1994**, *98*, 11623 – 11627.

[36] B. Le Guennic, D. Jacquemin, *Acc. Chem. Res.* **2015**, *48*, 530 – 537.

[37] S. Pascal, A. Haefele, C. Monnereau, A. Charaf-Eddin, D. Jacquemin, B. Le Guennic, C. Andraud, O. Maury, *J. Phys. Chem. A* **2015**, *119*, 4038 – 4047.

[38] K. Ohta, S. Yamada, K. Kamada, A. D. Slepkov, F. A. Hegmann, R. R. Tykwinski, L. D. Shirtcliff, M. M. Haley, P. Salek, F. Gel'mukhanov, H. Ågren, *J. Phys. Chem. A* **2011**, *115*, 105 – 117.

[39] S. Hirata, M. Head-Gordon, *Chem. Phys. Lett.* **1999**, *314*, 291 – 299.

[40] A. Faucon, R. Lenk, J. Hemez, E. Gautron, D. Jacquemin, J.-Y. Le Questel, J. Graton, A. Brosseau, E. Ishow, *Phys. Chem. Chem. Phys.* **2013**, *15*, 12748 – 12756.

[41] R. Orlowski, M. Banasiewicz, G. Clermont, F. Castet, R. Nazir, M. Blanchard-Desce, D. T. Gryko, *Phys. Chem. Chem. Phys.* **2015**, *17*, 23724 – 23731.

[42] a) I. I. Slowing, B. G. Trewyn, S. Giri, V. S. Y. Lin, *Adv.Funct. Mater.* **2007**, *17*, 1225 – 1236; b) M. W. Ambrogio, C. R. Thomas, Y.-L. Zhao, J. I. Zink, J. F. Stoddart, *Acc. Chem. Res.* **2011**, *44*, 903 – 913.

[43] D. Tarn, M. Xue, J. I. Zink, *Inorg. Chem.* **2013**, *52*, 2044 – 2049.

[44] A. Masoumi, B. Goldenson, S. Ghirmai, H. Avagyan, J. Zaghi, K. Abel, X. Zheng, A. Espinosa-Jeffrey, M. Mahanian, P. T. Liu, M. Hewison, M. Mizwicki, J. Cashman, M. Fiala, *J. Alzheimer's Dis.* **2009**, *17*, 703 – 717.

[45] P. Venkatesan, M. N. A. Rao, *J. Pharm. Pharmacol.* **2000**, *52*, 1123 – 1128.

[46] E. Kim, A. Felouat, E. Zaborova, J.-C. Ribierre, J. W. Wu, S. Senatore, C. Matthews, P.-F. Lenne, C. Baffert, A. Karapetyan, M. Giorgi, D. Jacquemin, M. Ponce-Vargas, B. Le Guennic, F. Fages, A. D'Aléo, *Org. Biomol. Chem.* **2016**, *14*, 1311 – 1324.

[47] K. Kamada, C. Hara, K. Ogawa, K. Ohta, Y. Kobuke, *Chem. Commun.* **2012**, *48*, 7988 – 7990.

[48] Gaussian 09, Revision D.01, M. J. Frisch, G. W. Trucks, H. B. Schlegel, G. E. Scuseria, M. A. Robb, J. R. Cheeseman, G. Scalmani, V. Barone, B. Mennucci, G. A. Petersson, H. Nakatsuji, M. Caricato, X. Li, H. P. Hratchian, A. F. Izmaylov, J. Bloino, G. Zheng, J. L. Sonnenberg, M. Hada, M. Ehara, K. Toyota, R. Fukuda, J. Hasegawa, M. Ishida, T. Nakajima, Y. Honda, O. Kitao, H. Nakai, T. Vreven, J. A. Montgomery, Jr., J. E. Peralta, F. Ogliaro, M. Bearpark, J. J. Heyd, E. Brothers, K. N. Kudin, V. N. Staroverov, T. Keith, R. Kobayashi, J. Normand, K. Raghavachari, A. Rendell, J. C. Burant, S. S. Iyengar, J. Tomasi, M. Cossi, N. Rega, J. M. Millam, M. Klene, J. E. Knox, J. B. Cross, V. Bakken, C. Adamo, J. Jaramillo, R. Gomperts, R. E. Stratmann, O. Yazyev, A. J. Austin, R. Cammi, C. Pomelli, J. W. Ochterski, R. L. Martin, K. Morokuma, V. G. Zakrzewski, G. A. Voth, P. Salvador, J. J. Dannenberg, S. Dapprich, A. D. Daniels, O. Farkas, J. B. Foresman, J. V. Ortiz, J. Cioslowski, D. J. Fox, Gaussian, Inc., Wallingford CT, **2013**.

[49] J. M. Tomasi, R. Cammi, *Chem. Rev.* **2005**, *105*, 2999 – 3093.

Received: December 4, 2015
Published online on February 25, 2016